## ARTICLE

Check for updates

# Sub-volt switching of nanoscale voltage-controlled perpendicular magnetic tunnel junctions

Yixin Shao [1], Victor Lopez-Dominguez [1], Noraica Davila[2], Qilong Sun[3], Nicholas Kioussis [4], Jordan A. Katine[2] & Pedram Khalili Amiri [1]✉

Magnetic random-access memory (MRAM) based on voltage-controlled magnetic anisotropy in magnetic tunnel junctions (MTJs) is a promising candidate for high-performance computing applications, due to its lower power consumption, higher bit density, and the ability to reduce the access transistor size when compared to conventional current-controlled spin-transfer torque MRAM. The key to realizing these advantages is to have a low MTJ switching voltage. Here, we report a perpendicular MTJ structure with a high voltage-controlled magnetic anisotropy coefficient ~130 fJ/Vm and high tunnel magnetoresistance exceeding 150%. Owing to the high voltage-controlled magnetic anisotropy coefficient, we demonstrate sub-nanosecond precessional switching of nanoscale MTJs with diameters of 50 and 70 nm, using a voltage lower than 1 V. We also show scaling of this switching mechanism down to 30 nm MTJs, with voltages close to 2 V. The results pave the path for the future development and application of voltage-controlled MRAMs and spintronic devices in emerging computing systems.

[1] Department of Electrical and Computer Engineering, Northwestern University, Evanston, IL 60208, USA. [2] Western Digital Corporation, San Jose, CA 95119, USA. [3] School of Science, Shandong Jianzhu University, 250101 Jinan, Shandong, China. [4] Department of Physics and Astronomy, California State University, Northridge, CA 91330, USA. ✉email: pedram@northwestern.edu

Magnetic random-access memory (MRAM) based on perpendicular magnetic tunnel junctions (MTJs) is being actively developed by the semiconductor industry, both as an embedded nonvolatile memory (eNVM) and for random-access (Cache) memory applications[1,2]. Its key advantages are its nonvolatile data retention, single-transistor cell structure, small number of added lithography masks (compared to embedded Flash), and compatibility with complementary metal oxide semiconductor (CMOS) processing[3,4]. One of the important requirements of embedded MRAM for Cache applications in microprocessors is the ability to switch the direction of the magnetization with high speed (~3–10 ns or less, for level 2 and level 3 Cache, respectively) and with low write voltage. The conventional switching mechanism based on current-induced magnetization reversal using spin-transfer torque (STT) requires significant current density through the MTJ (in particular, for high-speed switching), thus limiting its ability to scale the access transistor size[1,5–7]. Voltage-controlled magnetic anisotropy (VCMA) has been proposed as an alternative writing mechanism which, owing to its electric-field-based principle, may solve the limitations present in STT-MRAMs and enable higher bit density, as well as ultra-low power switching due to reduced Ohmic dissipation[8–13], in advanced CMOS nodes.

VCMA switching is realized by applying a voltage pulse across the MTJ, the length of which approximately corresponds to half the precession period of the MTJ free layer[8,11,13–25]. When a voltage of a particular polarity is applied, due to the VCMA effect[10,12,26–32], the energy barrier $E_b$ between the two stable free layer states is reduced. Once the voltage reaches a threshold value, the energy barrier is eliminated and the magnetic moment of the free layer starts to process around an in-plane axis. This axis is defined by a small external bias magnetic field in typical experiments, but can be replaced by a built-in static magnetic field in appropriately designed devices. By removing the voltage at the half-period point, the magnetization of the free layer will end up in the opposite direction.

One of the main requirements for the practical adoption of VCMA-MRAM is to have the device switched at low voltages, which are compatible with the voltage levels of existing CMOS logic circuits. The switching voltage in precessional VCMA switching, noted as $V_{sw}$, can be expressed as $V_{sw} = 4 t_{MgO}E_b(V=0)/(\pi\xi D^2)$[8,33], where $t_{MgO}$ is the thickness of the MgO tunnel barrier, $E_b$ is the energy barrier between the free layer states, $\xi$ is the VCMA coefficient which quantifies the sensitivity of the magnetic anisotropy to electric fields, and $D$ is the diameter of the device. Thus, because $V_{sw}$ is inversely proportional to $\xi$, a sufficiently large VCMA coefficient is essential to achieve switching of nanoscale MTJs with a low write voltage. Most previous works on VCMA-induced switching in MTJs utilized material stacks with relatively low VCMA values (~ 30–50 fJ/Vm), resulting in high switching voltages (~2 V or higher), and limiting the minimum MTJ diameters that could be switched to 50 nm or larger[13–15,17–25]. While subsequent works theoretically predicted[34–36] and even experimentally demonstrated[37–40] material structures with substantially higher VCMA values, none of these materials were implemented into precessional switching experiments on nanoscale MTJs. This has been due to the difficulty of simultaneously achieving all required MTJ parameters (in addition to high VCMA) in the same material stack, the most important being the tunnel magnetoresistance (TMR) ratio (required for electrical readout of the device state) and the perpendicular magnetic anisotropy (PMA), along with sufficient thermal tolerance (up to 400 °C) to withstand advanced CMOS back-end-of-line (BEOL) processing temperatures. In addition, some reports of large voltage-induced modulation of magnetic properties relied on magneto-ionic effects[41–53] which, while large,

generally do not function at the sub-nanosecond time scales required for high-speed precessional switching.

In this work, we demonstrate sub- 1 V switching of nanoscale MTJs using VCMA, and demonstrate scaling of this switching mechanism down to MTJs with 30 nm diameter. This is achieved by developing a voltage-controlled MTJ material stack which simultaneously provides large VCMA (~130 fJ/Vm), high TMR (>150%), and thermal annealing stability at 400 °C. We performed precessional VCMA switching experiments on nanoscale perpendicular MTJs made of this stack, with diameters ranging from 30 to 70 nm. Switching with higher than 90% probabilities in both directions was obtained on 50 and 70 nm MTJs with a voltage pulse amplitude of ~1 V, with a switching energy of ~11–15 fJ/bit. In agreement with the single-domain switching model, the switching voltage increased to ~2 V for the 30 nm MTJs, which is comparable to the best previously reported values for much larger MTJs (>50 nm). We also report ab initio electronic structure calculations of the VCMA effect in material stacks similar to those studied experimentally in this work, which shed light on the origins of the high VCMA and its effect on the observed transport characteristics. Overall, these results represent the lowest VCMA-induced switching voltage and the smallest VCMA-switched MTJ diameter, both while maintaining high TMR and temperature stability, in nanoscale MRAM devices reported to date.

## Results and discussion

**Device structure.** A schematic of the devices studied in this work is shown in Fig. 1a. The MTJ stack consists of bottom electrode / pinning layer (which includes a Co/Pt-based synthetic antiferromagnetic (SAF) multilayer) / $Co_{20}Fe_{60}B_{20}$ (0.8) / MgO (~1.5) / $Co_{17.5}Fe_{52.5}B_{30}$ (1.6) / Mo (5) / top electrode, where numbers in parentheses are thicknesses in nanometers. The total thickness of the stack, excluding its bottom and top electrodes, was ~20 nm. Devices were patterned into circular pillars with diameters of 30, 50, and 70 nm. More information about the sample preparation is given in Methods and in Supplementary Note 1.

The use of Mo as the capping layer was motivated by its better thermal annealing stability compared to alternative capping materials (notably, commonly used heavy metals such as Ta and Ir). This, in turn, is a consequence of the fact that Mo hardly bonds to Co or Fe, thus preventing its diffusion into the CoFeB layer[54–56]. Different CoFeB compositions were used in the top free and bottom fixed layers, varying the B content while keeping the same 1:3 ratio between Co and Fe. The Boron concentration in the bottom fixed CoFeB layer was chosen to be 20%, which has been shown to better promote the formation of (001) MgO texture[57,58], thus increasing the TMR. A higher B content of 30% was chosen for the top CoFeB layer. This is motivated by the fact that the composition ratio of Fe and B in $Co_{17.5}Fe_{52.5}B_{30}$ is closer to that of body-centered tetragonal $Fe_2B$. Thus, as noted previously in the case of in-plane MTJs with large B content in the CoFeB[58], a short-range ordered structure close to that of $Fe_2B$ can form in the free layer. This can induce a tensile strain on the MgO[58,59], which is expected to affect the VCMA[34]. Although the higher B content will result in reduced CoFeB crystallization and could be harmful for the TMR ratio[58], this is effectively compensated in the B-rich top free layer due to the fact that we can use a higher annealing temperature, enabled by the thermally stable Mo capping. In addition, we note that the MgO texture (hence TMR) is more prominently affected by the CoFeB layer preceding the MgO, which in our case contains only 20% Boron. In the following measurements, the positive voltage is defined as the voltage being applied to the top electrode relative to the bottom electrode. Figure 1b shows the device resistance as a function of the perpendicular magnetic field for a 70 nm MTJ
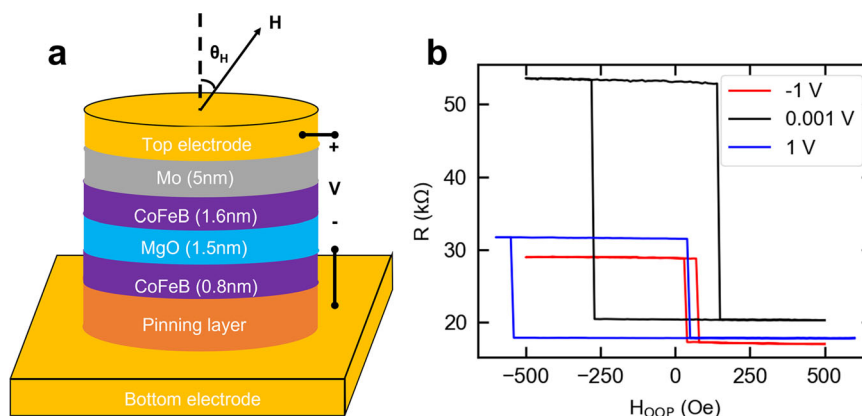
**Fig. 1 Device structure and magnetoresistance curves. a** Schematic of a magnetic tunnel junction used in this work. Positive voltage is defined as indicated in **a**. An external magnetic field ($H$) is applied at an angle $\theta_H$ from the film normal. **b** Resistance as a function of magnetic field for a 70 nm device under different DC bias voltages when $\theta_H = 0$. $H_{oop}$ denotes the out-of-plane magnetic field.

measured under different DC bias voltages. The low and high resistance levels correspond to the parallel (P) and antiparallel (AP) magnetization configurations of the two CoFeB layers, respectively. Since the magnetization of the bottom CoFeB (fixed reference layer) is fixed by the pinning layer, only the magnetization of the top CoFeB (free layer) can be switched. The TMR ratio, which is defined as $(R_{AP} - R_p)/R_p$, shows a value of ~170% in the loop measured at near-zero (1 mV) voltage bias. Negative (positive) 1 V bias voltages are observed to decrease (increase) the coercivity of the free layer, confirming the existence of VCMA. A small offset field of ~−50 Oe can be observed, which is due to the imperfect cancellation of the stray magnetic field from the SAF and reference layers.

**Voltage-induced switching measurements**. Electric-field-induced precessional switching measurements were performed on the patterned devices, using voltage pulses of different amplitude and width. A constant tilted magnetic field was applied at an angle $\theta_H$ from the film normal during measurement, to (i) compensate the offset (i.e., stray) field, (ii) define an in-plane axis for the precession, and (iii) adjust the energy barrier of different-sized devices to a similar value for fair comparison[60] of their switching behavior, similar to earlier reports of VCMA-induced switching[14,15]. The switching probability was obtained by measuring the device resistance after each voltage pulse application. Figure 2 shows the switching probability of successive back and forth switching (parallel state to antiparallel state and back to parallel, noted as $P_{010}$) for a 70 nm MTJ, which was obtained using $10^3$ switching attempts with identical voltage pulses, each having the nominal amplitude of 0.9 V, for various pulse widths and external fields. Data on MTJs with different diameters were in general agreement with those reported here, and are shown in Supplementary Note 2. The white dashed line in Fig. 2 indicates the in-plane magnetic field chosen for the switching measurements which are later shown in Fig. 3.

It should be noted that the actual pulse amplitude across the MTJ is higher than the nominal value, due to the reflection resulting from the impendence mismatch between the MTJs and the 50 Ω transmission line. As a result, the peak voltage across the MTJ is in fact $V = (1 + \Gamma)V_{nominal}$, where $\Gamma$ is the voltage reflection coefficient and $\Gamma \approx 1$ when the MTJ impedance is much larger than 50 Ω. Thus, in principle, for long enough square-shaped pulses, the actual peak voltage across the MTJ will be $V \approx 2V_{nominal}$. However, due to the finite rise time of the pulse generator used in this experiment, short (sub-ns) pulses were nearly triangular in shape and thus the actual amplitude across

the MTJ was significantly smaller than $2V_{nominal}$. To accurately determine its value, the actual pulse shapes were measured using an oscilloscope with a 1 MΩ input impendence, representing a reflection coefficient $\Gamma \approx 1$, similar to the MTJ case. All switching voltages reported in this paper correspond to this calibrated peak value.

To investigate the switching behavior in more detail, we next measured the probabilities of parallel to antiparallel ($P_{01}$), antiparallel to parallel ($P_{10}$), and consecutive back and forth switching ($P_{010}$) for the same 70 nm device, using the fixed external field determined from Fig. 2, under different nominal voltage amplitudes and write pulse durations. The results are shown in Fig. 3, where the switching probabilities were determined using a larger number of write attempts ($10^4$ attempts for each pulse amplitude and duration) compared to Fig. 2. Oscillations of the switching probability as a function of pulse width were observed for voltages over 0.8 V, indicating the electric-field-induced precessional switching[8,11,13–15,17–25]. Switching with > 90% probabilities in both directions ($P_{01} > 90$, $P_{10} > 90$, $P_{010} > 81\%$) was achieved at a 0.9 V nominal amplitude and 0.4 ns pulse duration. It is worth noting that the switching probabilities for the two directions are not exactly the same, especially at lower voltages. This is because of the imperfect compensation of the stray field from the fixed layer, and the finite voltage-dependent effect of spin-transfer torque (which is also evident from the shifts in the hysteresis loops shown in Fig. 1b). During the measurement, a tilted external magnetic field was applied with the perpendicular component set to compensate both the stray field from the fixed layer and the shift due to STT near the switching voltage. However, since the shift induced by STT depends on the applied current (voltage), the switching probabilities in the two directions show a larger difference at lower voltages, where the STT effect is smaller.

The (nearly triangular) real shape of the voltage pulse at this point, recorded using the oscilloscope, is shown in the inset in Fig. 3c, showing a maximum amplitude of $V_{sw} = 0.95$ V. Here, the black dots correspond to the measured data, and the red dashed line is a Gaussian fit to the data. This value of $V_{sw}$ is ~2× lower than the best previously reported values for precessional VCMA switching in MTJs[11,13–15,17–23]. The energy dissipation during the switching was calculated using the fitted Gaussian function, and is given by $E = \int P dt = \int (V^2/R) dt = 15.1$ fJ/bit, where the resistance was chosen as $R = (R_P + R_{AP})/2$ under −1 V DC bias, as shown in Fig. 1b, to obtain the average energy for the two switching directions. The same measurements, repeated on MTJs with different sizes on the same wafer gave results of $V_{sw} = 1.05$ V, $E = 11.2$ fJ/bit for 50 nm MTJs, and $V_{sw} = 2$ V, $E = 17.6$ fJ/bit for
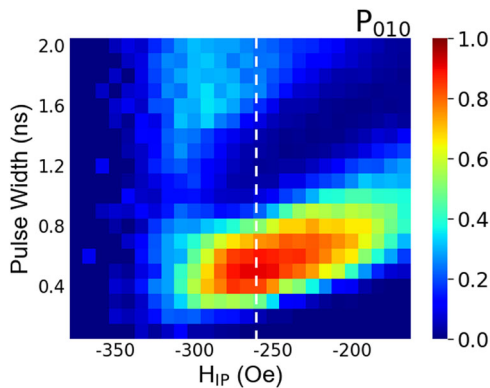
**Fig. 2 Switching phase diagram for a 70 nm device.** Measured probability of back and forth switching (i.e., two successful consecutive switching attempts) for a 0.9 V nominal voltage pulse under different pulse widths and in-plane magnetic fields applied to a 70 nm device. The dashed white line indicates the in-plane magnetic field that was used for the subsequent switching probability measurements as a function of voltage pulse amplitude and width, shown in Fig. 3.

30 nm MTJs. More information on the latter two cases is given in Supplementary Note 2. The energy consumption per write is comparable to the best previously reported values for VCMA switching[14–17], and could be further reduced by designing MTJ stacks with a higher resistance-area (RA) product.

**Determination of VCMA coefficient.** Next, we extracted the VCMA coefficients for the MTJs with different diameters from the switching measurement results. To do so, we first determined the energy barrier of the free layer under near-zero bias, $E_b(V=0)$, by measuring the mean time for thermally activated switching (i.e., the dwell time)[61]. To obtain the energy barrier under the same condition as in the switching measurements, the dwell time measurements were performed on the same devices and under the exact same applied external field as in the switching measurements described above. The dwell time was determined from a total of ~300 switching events, by monitoring the real-time voltage across the MTJ using an oscilloscope. Results from a 70 nm device are shown in Fig. 4a and b. The energy barrier $E_b$ was calculated from $\tau = \tau_0 exp(E_b/k_B T)$[61], where $\tau$ was the measured dwell time, $\tau_0$ is the attempt time (assumed to be 1 ns), $k_B$ is Boltzmann's constant, and $T$ is temperature. The parallel state distribution corresponded to a dwell time of $\tau_P = 19.2$ s as shown in Fig. 4b, resulting in an energy barrier of $E_b(V=0) = 23.7$ $k_B T$, while the same calculation performed on the AP state gave $E_b(V=0) = 22.7$ $k_B T$. As mentioned above, the small asymmetry can be attributed to the finite remaining stray field[62] from the fixed layer, which is not perfectly canceled by the applied field. Thus, the energy barrier under zero bias was estimated as $E_b(V=0) = 23.2 \pm 0.5$ $k_B T$. Similarly, the energy barriers for the 30 and 50 nm devices reported in this work were measured to be $23.5 \pm 0.5$ $k_B T$ and $22.4 \pm 0.8$ $k_B T$, respectively. As mentioned above, the similar energy barrier for devices of different sizes was the result of adjusting the in-plane external field, to allow a fair comparison of their switching voltages.

Independently, the energy barrier can be calculated as the product of an effective anisotropy energy density $K_{eff}$ and the free layer volume $V$, where $V = (t_{CoFeB}D^2\pi)/4$ and $K_{eff} = K_i/t_{CoFeB} - 2\pi M_s^2$ [8,33,63]. Here, $t_{CoFeB}$ is the free layer thickness, $K_i$ is the interfacial anisotropy energy density, and $M_s$ is the saturation magnetization. Assuming a linear dependence of the

interfacial anisotropy energy density on voltage, we have $K_i(V) = \xi V/t_{MgO} + K_i(V=0)$. Combining the above equations, the voltage-dependent energy barrier can then be written as[8,33]

$$\frac{E_b(V)}{D^2} = \xi \frac{\pi}{4t_{MgO}} V + \frac{E_b(V=0)}{D^2} \qquad (1)$$

At the threshold voltage for precessional reversal, the energy barrier becomes zero, i.e., $E_b(V_{sw}) = 0$. The VCMA coefficient can thus be determined from Eq. (1), using the $E_b(V=0)$ values measured above for MTJs with different diameters. Red dots in Fig. 4c show the VCMA coefficients for MTJs with different diameters, obtained using this method. The values calculated for 30, 50, and 70 nm devices were 102, 67, and 39 fJ/Vm, respectively.

The VCMA coefficients extracted from the precessional switching experiments decrease noticeably with increasing MTJ diameter. This can be attributed to the role of sub-volume nucleation in determining the energy barrier of MTJs with larger diameters[60,64–67], which has been shown in previous works to result in an underestimation of the VCMA coefficient obtained from pulsed switching measurements for large MTJs[60]. Specifically, in free layers with larger diameters (typically > 40 nm), the thermally activated switching (which was used here to determine the dwell time) is no longer realized as a single-domain reorientation, since there are more energetically favorable paths for the magnetization to reverse through the formation of a nonuniform micromagnetic configuration. Hence, the effective free layer diameter which determines $E_b$ will be smaller than its real value (50 or 70 nm). Since this effect is not accounted for in Eq. (1), using this expression to estimate the VCMA value for our 50 and 70 nm devices results in a lower (underestimated) VCMA coefficient.

To verify this hypothesis, we performed complementary measurements of the VCMA coefficient, which are discussed in detail in Supplementary Note 5. We first extracted the effective area for MTJs with different sizes by measuring the free layer energy barrier at different in-plane magnetic fields. Then, by substituting this effective area (which accounts for the sub-volume nucleation effect) into Eq. (1), we obtained VCMA coefficients of 81, 106, and 99 fJ/Vm for 30, 50, and 70 nm devices, respectively. These coefficients are indicated with blue squares in Fig. 4c.

In addition, we independently determined the VCMA coefficient for each device diameter by measuring the voltage dependence of the free layer energy barrier. This independent measurement resulted in VCMA coefficients of 128, 131, and 100 fJ/Vm for the 30, 50, and 70 nm devices, respectively. These coefficients are indicated with green diamonds in Fig. 4c. The values obtained from the voltage-dependent energy barrier measurement are in general higher than the values extracted from the switching measurements. We attribute this to the effect of the pulse shape on the switching dynamics[68]: Since the estimation of VCMA from the switching data assumes a constant (square-shaped) voltage pulse, the non-ideal pulse shape in the experiment (inset of Fig. 3c) results in an underestimation of the VCMA coefficient. This artefact is not present in the voltage-dependent energy barrier measurements, making their resulting VCMA coefficients more reliable.

It is worth comparing the switching results of this work with those from a previous report[14], where a switching voltage of 1.96 V was achieved on a $D = 50$ nm MTJ with a VCMA coefficient of $\xi = 32$ fJ/Vm and an energy barrier similar to this work (~23 $k_B T$)[14,60]. Based on Eq. (1), the switching voltage can be expressed as $V_{sw} = 4t_{MgO}E_b(V=0)/(\pi\xi D^2)$. Comparing these
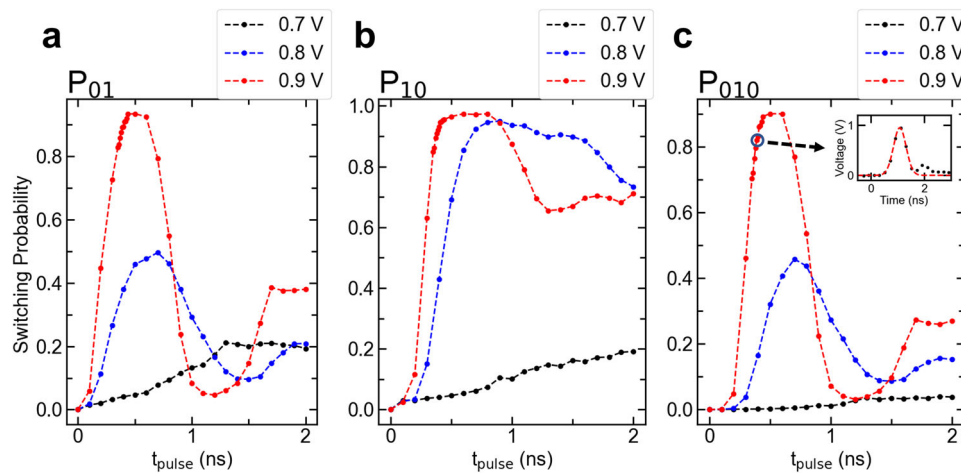
**Fig. 3 Measured switching probabilities for a 70 nm device.** Switching probabilities **a** from parallel to antiparallel ($P_{01}$), **b** antiparallel to parallel ($P_{10}$), and **c** back and forth switching ($P_{010}$) under different voltage pulses, as a function of pulse duration. The inset in **c** shows the measured shape of the pulse with 0.9 V nominal amplitude and 0.4 ns width, which gives >90% switching probability in both directions. The black dots are measured using an oscilloscope with a 1 MΩ impedance, and the red dashed line is a Gaussian fit to the data.

data to the switching results from 30 nm MTJs in the present work (Supplementary Note 2), we note that given the comparable $t_{MgO}$ and $E_b(V=0)$, the switching voltage should be inversely proportional to $\xi D^2$. Thus, for our $D = 30$ nm MTJs with average $\xi = 102$ fJ/Vm, one would expect the switching voltage to be ~1.7 V. For comparison, note that the estimated switching voltage would be ~5.4 V assuming a 30 nm MTJ with $\xi = 32$ fJ/Vm, which would break the MgO barrier before inducing switching. It is worth noting that another recent work[25] reported VCMA and TMR values comparable to those presented here, but in significantly larger MTJs with 100 nm diameter, and using a different approach to engineer the MTJ material stack, i.e., by engineering the interfacial spin-orbit coupling using an unspecified transition metal layer insertion at the free layer—MgO interface. However, a more detailed comparison to this work is not possible, since it did not report the switching voltage amplitude, the measurement method used to determine the VCMA coefficient, or the type of the transition metal layer used in the experiment. Finally, we note that while the 70 nm device data in Fig. 3 show switching probabilities ($P$) higher than 90%, we also performed switching probability measurements at voltages up to 1.5 V, where much lower write error rate (WER = $1 - P$), approaching ~$10^{-3}$, was observed. These results, which are shown in Supplementary Note 4, are comparable to WER results obtained at significantly larger write voltages in earlier VCMA switching experiments. A more detailed comparison with other recent works on precessional VCMA switching is given in Supplementary Note 3.

**Ab initio calculations**. To further understand the effect of Mo capping on the PMA and VCMA, ab initio electronic structure calculations were carried out in a Mo/CoFe/MgO heterostructure. The slab supercell for the Mo/CoFe/MgO (001) junction consisted of three Mo monolayers on top of three monolayers of $B_2$-type CoFe, sandwiched between seven monolayers of rocksalt MgO and a 15 Å-thick vacuum region. The O atoms at the CoFe/MgO interface were placed atop the Fe atoms, which is the most stable configuration. We denote with $Fe_1$ and $Fe_2$ the atoms at the Fe/MgO and Fe/Mo interfaces, respectively.

The $Fe_1$, $Fe_2$, and Co magnetic moments were 2.683, 2.146, and 1.769 $\mu_B$, respectively. Induced magnetization was also found in the capped Mo monolayers because of the proximity effect, where the interfacial Mo monolayer acquires a spin moment of $-0.180$

$\mu_B$. The variation of the magneto-crystalline anisotropy (MCA) as a function of the electric field in MgO is shown in Fig. 5a, which exhibits an asymmetric (shifted) V-shape with giant $\xi$ values of $+479$ and $-512$ fJ/Vm, and a minimum near 0.2 V/nm. The underlying origin of the shifted V-shape arises from the fact that the interface bands depend on the magnetization direction due to the Rashba effect. The Rashba coupling, which is proportional to the net electric field, $E_z$, at the interface, has contributions from both the internal and external electric fields[69]. The critical field where the anisotropy reaches its maximum or minimum value depends on the interplay between the two electric fields, where the internal electric field can be tuned via strain and/or disorder. Thus, this critical electric field depends sensitively on the biaxial strain which is ubiquitous in heavy metal/ferromagnet/insulator tunnel junctions, and as noted before, may be further affected by the presence of remaining B atoms within the free layer after annealing[70]. Further simulations showed that a small change in the in-plane lattice constant of CoFe (0.5%) would shift the critical electric field by several tenths of V/nm, and from negative to positive. Furthermore, disorder at the CoFe/MgO and Mo/CoFe interfaces can change both the value of $\xi$ and the critical electric field where the anisotropy reaches its minimum. Thus, we hypothesize that in experiments, the real lattice constant may shift the minimum point out of the range of the experimentally accessible electric fields, resulting in an apparently monotonic dependence.

In order to understand the underlying mechanism of both the anisotropy and VCMA behavior, we calculated the difference in spin-orbit coupling (SOC) energies between the in- ($\parallel$) and out-of-plane ($\perp$) magnetization orientations, $\Delta E_{SOC} = (E_{SOC}^{\parallel} - E_{SOC}^{\perp})$[71]. We find that the MCA $\approx \Delta E_{SOC}$ due to the relatively small SOC of Mo. In Fig. 5b we show the layer-resolved and total electric-field-induced change of $\Delta E_{SOC}$, $\delta_{SOC} = \Delta E_{SOC}(\overrightarrow{E}) - \Delta E_{SOC}(\overrightarrow{E}_c)$, where $\overrightarrow{E}_c$ is the critical electric field. The layer-resolved $\delta_{SOC}$ for $\overrightarrow{E} > \overrightarrow{E}_c$ and $\overrightarrow{E} < \overrightarrow{E}_c$ is consistent with the trend of the electric field variation of the anisotropy in Fig. 5b, indicating that the largest contribution to electric-field-induced change of $\Delta E_{SOC}$ arises from the interfacial Mo layer.

**Conclusions**

In summary, a Mo-capped bottom-pinned voltage-controlled MTJ structure has been demonstrated, with simultaneously high
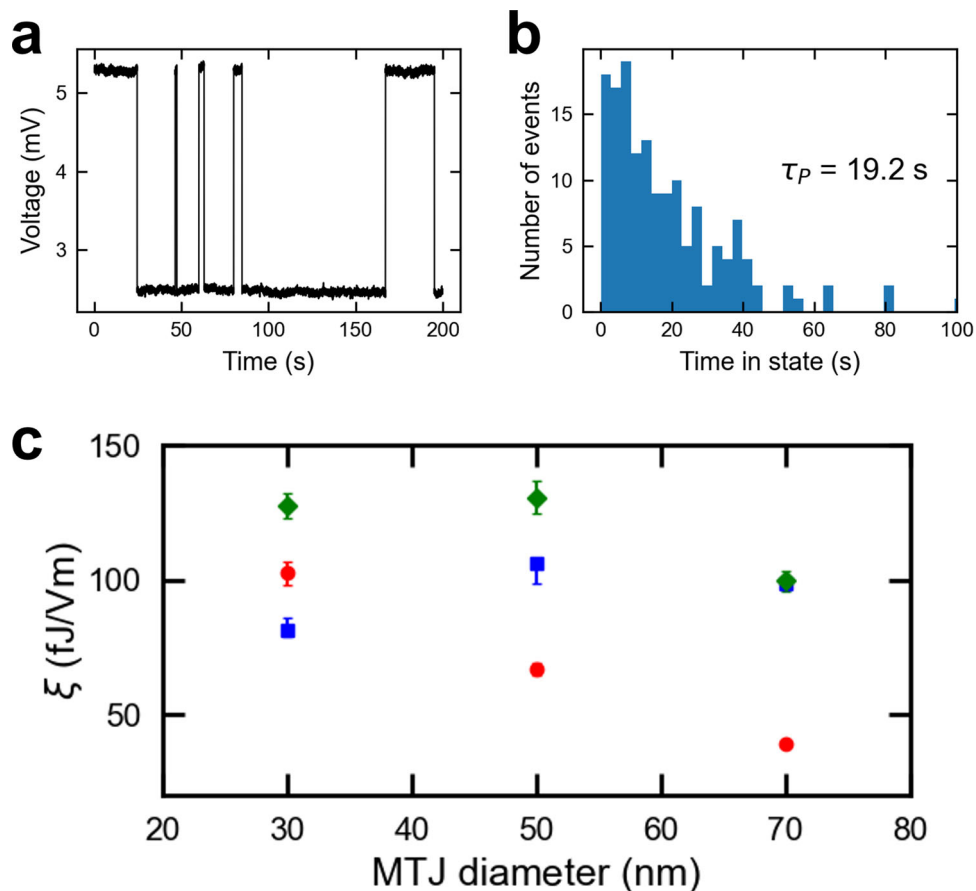
**Fig. 4 Characterization of free layer energy barrier and VCMA coefficients. a** Real-time voltage measured for near-zero bias across the 70 nm MTJ, under the same applied field used for the switching measurements in Fig. 3. **b** Distribution for parallel state dwell times for the same device. **c** Red dots: VCMA coefficients obtained from the switching voltages. Error bars represent the uncertainty in the energy barrier measured from the dwell time. Blue squares: VCMA coefficients obtained from the switching voltages, using the effective MTJ area for each diameter (See Supplementary Note 5 for details). Error bars represent the uncertainty in the energy barrier measured from the dwell time, and th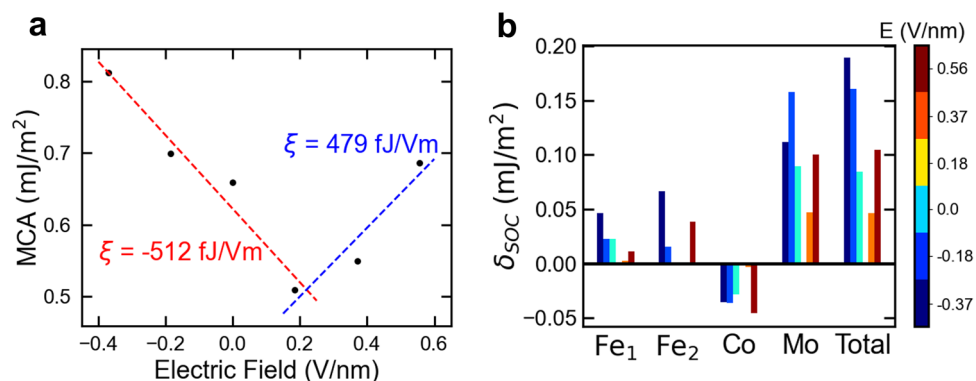e fitting parameters used to estimate the effective area. Green diamonds: VCMA coefficients obtained from the voltage-dependent energy barrier measurements (See Supplementary Note 5 for details). Error bars represent the uncertainty in the energy barrier measured from the dwell time, and the fitting parameters used to estimate the effective area.



**Fig. 5 Ab initio electronic structure calculations of anisotropy and VCMA. a** Magnetic anisotropy as a function of electric field in MgO for the Mo/FeCo/MgO junction. **b** The E-field-induced change of SOC energy difference ($\delta_{SOC}$) for the Mo/FeCo/MgO junction. The atom-resolved $\delta_{SOC}$ is also shown.

VCMA coefficient and TMR. Using this material structure, VCMA switching of nanoscale MTJs has been achieved with a switching voltage lower than 1 V. We also demonstrated scaling of the precessional VCMA switching mechanism down to 30 nm MTJs, pointing to the potential of VCMA-controlled MTJs for high-density MRAM arrays. The role of the Mo capping was further investigated by ab initio calculations, which indicate the importance of local strain on the size and qualitative features of the VCMA effect. Our results provide a promising direction for VCMA-MRAM in embedded memory applications, making voltage-controlled MTJs compatible with the standard voltage levels of logic transistors.

## Methods

**Device fabrication.** The 1.6 nm-thick CoFeB free layers for all the MTJs used in this work were taken from a wedged film where the CoFeB thickness was varied across the wafer. The film stacks were sputter deposited in an ultrahigh vacuum (UHV) physical vapor deposition (PVD) system (Canon ANELVA HC7100), annealed at wafer level for 30 min at 400 °C, and then fabricated into circular pillars with diameters of 30, 50, and 70 nm using electron beam lithography. The MgO layers were deposited by radio-frequency (RF) sputtering, while metallic layers were deposited by DC sputtering.

**Electrical measurements.** Electrical measurements were performed on a probe station with a projected field electromagnet, using microwave probes with a ground-signal-ground (GSG) configuration. The voltage pulses for the switching measurement were applied with a Tektronix pulse generator (PSPL10070A), and the resistance after each pulse was measured by a sourcemeter (Keithley 2401) using a bias tee. Switching measurements were performed on three MTJs of each size.

**Ab initio calculations.** The first-principles calculations were carried out within the projector augmented-wave method[72], as implemented in the Vienna ab initio simulation package (VASP)[73]. The generalized gradient approximation was used to describe the exchange-correlation functional as parametrized by Perdew, Burke, and Ernzerhof (PBE)[74]. The in-plane lattice constant was set to be 2.86 Å. An energy cutoff of 500 eV and a $16 \times 16 \times 1$ $k$-point mesh were used to relax the atomic coordinates for each electric field until the largest force became less than $5 \times 10^{-3}$ eV/Å, and the change in the total energy between two ionic relaxation steps was smaller than $10^{-6}$ eV. The dipole corrections were taken into account along the [001] direction. The SOC of the valence electrons was in turn included using the second-variation method[75] employing the scalar-relativistic eigenfunctions of the valence states and a $32 \times 32 \times 1$ $k$-point mesh. The MCA energy per unit interfacial area, $A$, was then determined from $(E_{[100]} - E_{[001]})/A$, where $E_{[100]}$ and $E_{[001]}$ are the total energies with magnetization along the [100] and [001] directions, respectively. The voltage-controlled magnetic anisotropy was calculated as $\Delta(\text{MCA}) = \xi E_I = \xi E_{ext}/\varepsilon$, where $\varepsilon$ is the dielectric constant of the insulator which depends on strain, and $E_{ext}$ is the external electric field[70,76].

## Data availability

## References

1. Chun, K. C. et al. A scaling roadmap and performance evaluation of in-plane and perpendicular MTJ based STT-MRAMs for high-density cache memory. *IEEE J. Solid State Circ.* **48**, 598–610 (2012).
2. Oboril, F., Bishnoi, R., Ebrahimi, M. & Tahoori, M. B. Evaluation of hybrid memory technologies using SOT-MRAM for on-chip cache hierarchy. *IEEE Trans. Computer Aided Des. Integr. Circ. Syst.* **34**, 367–380 (2015).
3. Åkerman, J. Toward a universal memory. *Science* **308**, 508–510 (2005).
4. Zhu, J.-G. Magnetoresistive random access memory: the path to competitiveness and scalability. *Proc. IEEE* **96**, 1786–1798 (2008).
5. Zhao, W. et al. Failure and reliability analysis of STT-MRAM. *Microelectr. Reliab.* **52**, 1848–1852 (2012).
6. Ralph, D. C. & Stiles, M. D. Spin transfer torques. *J. Magn. Magn. Mater.* **320**, 1190–1216 (2008).
7. Brataas, A., Kent, A. D. & Ohno, H. Current-induced torques in magnetic materials. *Nat. Mater.* **11**, 372–381 (2012).
8. Amiri, P. K. et al. Electric-field-controlled magnetoelectric RAM: progress, challenges, and scaling. *IEEE Trans. Magn.* **51**, 1–7 (2015).
9. Wang, W.-G., Li, M., Hageman, S. & Chien, C. Electric-field-assisted switching in magnetic tunnel junctions. *Nat. Mater.* **11**, 64–68 (2012).
10. Weisheit, M. et al. Electric field-induced modification of magnetism in thin-film ferromagnets. *Science* **315**, 349–351 (2007).
11. Shiota, Y. et al. Induction of coherent magnetization switching in a few atomic layers of FeCo using voltage pulses. *Nat. Mater.* **11**, 39–43 (2012).
12. Maruyama, T. et al. Large voltage-induced magnetic anisotropy change in a few atomic layers of iron. *Nat. Nanotechnol.* **4**, 158–161 (2009).
13. Kanai, S. et al. Electric field-induced magnetization reversal in a perpendicular-anisotropy CoFeB-MgO magnetic tunnel junction. *Appl. Phys. Lett.* **101**, 122403 (2012).
14. Grezes, C. et al. Ultra-low switching energy and scaling in electric-field-controlled nanoscale magnetic tunnel junctions with high resistance-area product. *Appl. Phys. Lett.* **108**, 012403 (2016).
15. Shiota, Y. et al. Pulse voltage-induced dynamic magnetization switching in magnetic tunneling junctions with high resistance-area product. *Appl. Phys. Lett.* **101**, 102406 (2012).
16. Wang, W. & Chien, C. Voltage-induced switching in magnetic tunnel junctions with perpendicular magnetic anisotropy. *J. Phys. D Appl. Phys.* **46**, 074004 (2013).
17. Kanai, S. et al. In-plane magnetic field dependence of electric field-induced magnetization switching. *Appl. Phys. Lett.* **103**, 072408 (2013).
18. Shiota, Y. et al. Evaluation of write error rate for voltage-driven dynamic magnetization switching in magnetic tunnel junctions with perpendicular magnetization. *Appl. Phys. Exp.* **9**, 013001 (2015).
19. Grezes, C. et al. Write error rate and read disturbance in electric-field-controlled magnetic random-access memory. *IEEE Magn. Lett.* **8**, 1–5 (2016).
20. Kanai, S., Matsukura, F. & Ohno, H. Electric-field-induced magnetization switching in CoFeB/MgO magnetic tunnel junctions with high junction resistance. *Appl. Phys. Lett.* **108**, 192406 (2016).
21. Shiota, Y. et al. Reduction in write error rate of voltage-driven dynamic magnetization switching by improving thermal stability factor. *Appl. Phys. Lett.* **111**, 022408 (2017).
22. Yamamoto, T. et al. Write-error reduction of voltage-torque-driven magnetization switching by a controlled voltage pulse. *Phys. Rev. Appl.* **11**, 014013 (2019).
23. Yamamoto, T. et al. Improvement of write error rate in voltage-driven magnetization switching. *J. Phys. D: Appl. Phys.* **52**, 164001 (2019).
24. Wu, Y. et al. Deterministic and Field-Free Voltage-Controlled MRAM for High Performance and Low Power Applications. In *2020 IEEE Symposium on VLSI Technology.* 1-2 (IEEE, 2020).
25. Carpenter, R. et al. Demonstration of a Free-layer Developed With Atomistic Simulations Enabling BEOL Compatible VCMA-MRAM with a Coefficient ≥100fJ/Vm. in *IEEE International Electron Devices Meeting 2021* (IEEE, 2021).
26. Rondinelli, J. M., Stengel, M. & Spaldin, N. A. Carrier-mediated magnetoelectricity in complex oxide heterostructures. *Nat. Nanotechnol.* **3**, 46–50 (2008).
27. Duan, C.-G. et al. Surface magnetoelectric effect in ferromagnetic metal films. *Phys. Rev. Lett.* **101**, 137201 (2008).
28. Duan, C.-G., Jaswal, S. S. & Tsymbal, E. Y. Predicted magnetoelectric effect in Fe/BaTiO 3 multilayers: ferroelectric control of magnetism. *Phys. Rev. Lett.* **97**, 047201 (2006).
29. Tsujikawa, M. & Oda, T. Finite electric field effects in the large perpendicular magnetic anisotropy surface Pt/Fe/Pt (001): a first-principles study. *Phys. Rev. Lett.* **102**, 247203 (2009).
30. Miwa, S. et al. Voltage controlled interfacial magnetism through platinum orbits. *Nat. Commun.* **8**, 1–9 (2017).
31. Niranjan, M. K., Duan, C.-G., Jaswal, S. S. & Tsymbal, E. Y. Electric field effect on magnetization at the Fe/MgO (001) interface. *Appl. Phys. Lett.* **96**, 222504 (2010).
32. Nakamura, K. et al. Giant modification of the magnetocrystalline anisotropy in transition-metal monolayers by an external electric field. *Phys. Rev. Lett.* **102**, 187201 (2009).
33. Vinasco, J. G. A. *Voltage-controlled Magnetic Dynamics in Nanoscale Magnetic Tunnel Junctions.* (University of California, 2014).
34. Kwon, S. et al. Colossal electric field control of magnetic anisotropy at ferromagnetic interfaces induced by iridium overlayer. *Phys. Rev. B* **99**, 064434 (2019).
35. Kwon, S. et al. Voltage-controlled magnetic anisotropy in heterostructures with atomically thin heavy metals. *Phys. Rev. Appl.* **12**, 044075 (2019).
36. Nakamura, K. et al. Effect of heavy-metal insertions at Fe/MgO interfaces on electric-field-induced modification of magnetocrystalline anisotropy. *J. Magn. Magn. Mater.* **429**, 214–220 (2017).
37. Kato, Y. et al. Giant voltage-controlled magnetic anisotropy effect in a crystallographically strained CoFe system. *Appl. Phys. Exp.* **11**, 053007 (2018).
38. Nozaki, T. et al. Highly efficient voltage control of spin and enhanced interfacial perpendicular magnetic anisotropy in iridium-doped Fe/MgO magnetic tunnel junctions. *NPG Asia Mater.* **9**, e451–e451 (2017).
39. Nozaki, T. et al. Voltage-controlled magnetic anisotropy in an ultrathin Ir-doped Fe layer with a CoFe termination layer. *APL Mater.* **8**, 011108 (2020).
40. Nozaki, T. et al. Enhancement in the interfacial perpendicular magnetic anisotropy and the voltage-controlled magnetic anisotropy by heavy metal doping at the Fe/MgO interface. *APL Mater.* **6**, 026101 (2018).
41. Bauer, U. et al. Magneto-ionic control of interfacial magnetism. *Nat. Mater.* **14**, 174–181 (2015).
42. Duschek, K., Uhlemann, M., Schlörb, H., Nielsch, K. & Leistner, K. Electrochemical and in situ magnetic study of iron/iron oxide films oxidized and reduced in KOH solution for magneto-ionic switching. *Electrochem. Commun.* **72**, 153–156 (2016).

43. Gilbert, D. A. et al. Structural and magnetic depth profiles of magneto-ionic heterostructures beyond the interface limit. *Nat. Commun.* **7**, 1–8 (2016).

44. Zhu, X. et al. In situ nanoscale electric field control of magnetism by nanoionics. *Adv. Mater.* **28**, 7658–7665 (2016).

45. Bauer, U., Emori, S. & Beach, G. S. Voltage-controlled domain wall traps in ferromagnetic nanowires. *Nat. Nanotechnol.* **8**, 411–416 (2013).

46. Bi, C. et al. Reversible control of Co magnetism by voltage-induced oxidation. *Phys. Rev. Lett.* **113**, 267202 (2014).

47. Di, N. et al. Influence of controlled surface oxidation on the magnetic anisotropy of Co ultrathin films. *Appl. Phys. Lett.* **106**, 122405 (2015).

48. Gilbert, D. A. et al. Controllable positive exchange bias via redox-driven oxygen migration. *Nat. Commun.* **7**, 1–8 (2016).

49. Grutter, A. J. et al. Reversible control of magnetism in La0. 67Sr0. 33MnO3 through chemically-induced oxygen migration. *Appl. Phys. Lett.* **108**, 082405 (2016).

50. Li, H.-B. et al. Electric-field control of ferromagnetism through oxygen ion gating. *Nat. Commun.* **8**, 1–7 (2017).

51. Walter, J. et al. Ion-gel-gating-induced oxygen vacancy formation in epitaxial L a 0.5 S r 0.5 Co O 3− δ films from in operando x-ray and neutron scattering. *Phys. Rev. Mater.* **1**, 071403 (2017).

52. Dasgupta, S. et al. Toward on-and-off magnetism: reversible electrochemistry to control magnetic phase transitions in spinel ferrites. *Adv. Funct. Mater.* **26**, 7507–7515 (2016).

53. Walter, J., Wang, H., Luo, B., Frisbie, C. D. & Leighton, C. Electrostatic versus electrochemical doping and control of ferromagnetism in ion-gel-gated ultrathin La0. 5Sr0. 5CoO3− δ. *ACS Nano* **10**, 7799–7810 (2016).

54. Liu, T., Zhang, Y., Cai, J. & Pan, H. Thermally robust Mo/CoFeB/MgO trilayers with strong perpendicular magnetic anisotropy. *Sci. Rep.* **4**, 1–6 (2014).

55. Almasi, H. et al. Enhanced tunneling magnetoresistance and perpendicular magnetic anisotropy in Mo/CoFeB/MgO magnetic tunnel junctions. *Appl. Phys. Lett.* **106**, 182406 (2015).

56. Li, X. et al. Predictive materials design of magnetic random-access memory based on nanoscale atomic structure and element distribution. *Nano Lett.* **19**, 8621–8629 (2019).

57. Yuasa, S., Suzuki, Y., Katayama, T. & Ando, K. Characterization of growth and crystallization processes in CoFeB∕ MgO∕ CoFeB magnetic tunnel junction structure by reflective high-energy electron diffraction. *Appl. Phys. Lett.* **87**, 242503 (2005).

58. Kodzuka, M. et al. Effects of boron composition on tunneling magnetoresistance ratio and microstructure of CoFeB/MgO/CoFeB pseudo-spin-valve magnetic tunnel junctions. *J. Appl. Phys.* **111**, 043913 (2012).

59. Villars, P. & Cenzual, K. *Pearson's crystal data®: crystal structure database for inorganic compounds*. (ASM International Materials Park, 2007).

60. Grezes, C. et al. In-plane magnetic field effect on switching voltage and thermal stability in electric-field-controlled perpendicular magnetic tunnel junctions. *AIP Adv.* **6**, 075014 (2016).

61. Brown, W. F. Jr Thermal fluctuations of a single-domain particle. *Phys. Rev.* **130**, 1677 (1963).

62. Rippard, W., Heindl, R., Pufall, M., Russek, S. & Kos, A. Thermal relaxation rates of magnetic nanoparticles in the presence of magnetic fields and spin-transfer effects. *Phys. Rev. B* **84**, 064439 (2011).

63. Khalili Amiri, P. et al. Switching current reduction using perpendicular anisotropy in CoFeB–MgO magnetic tunnel junctions. *Appl. Phys. Lett.* **98**, 112507, https://doi.org/10.1063/1.3567780 (2011).

64. Sun, J. et al. Effect of subvolume excitation and spin-torque efficiency on magnetic switching. *Phys. Rev. B* **84**, 064413 (2011).

65. Sato, H. et al. Junction size effect on switching current and thermal stability in CoFeB/MgO perpendicular magnetic tunnel junctions. *Appl. Phys. Lett.* **99**, 042501 (2011).

66. Sato, H. et al. Properties of magnetic tunnel junctions with a MgO/CoFeB/Ta/CoFeB/MgO recording structure down to junction diameter of 11 nm. *Appl. Phys. Lett.* **105**, 062403 (2014).

67. Hoffman, S., Tserkovnyak, Y., Khalili Amiri, P. & Wang, K. L. Magnetic bit stability: competition between domain-wall and monodomain switching. *Appl. Phys. Lett.* **100**, 212406 (2012).

68. Lee, H. et al. A word line pulse circuit technique for reliable magnetoelectric random access memory. *IEEE Trans. Very Large Scale Integr. Syst.* **25**, 2027–2034 (2017).

69. Barnes, S. E., Ieda, J. I. & Maekawa, S. Rashba spin-orbit anisotropy and the electric field control of magnetism. *Sci. Rep.* **4**, 1–5 (2014).

70. Ong, P. et al. Giant voltage modulation of magnetic anisotropy in strained heavy metal/magnet/insulator heterostructures. *Phys. Rev. B* **92**, 020407 (2015).

71. Sun, Q., Kwon, S., Stamenova, M., Sanvito, S. & Kioussis, N. Electric field modulation of magnetism in ferrimagnetic Heusler heterostructures. *Phys. Rev. B* **101**, 134419 (2020).

72. Blöchl, P. E. Projector augmented-wave method. *Phys. Rev. B* **50**, 17953 (1994).

73. Kresse, G. & Furthmüller, J. Efficient iterative schemes for ab initio total-energy calculations using a plane-wave basis set. *Phys. Rev. B* **54**, 11169 (1996).

74. Perdew, J. P., Burke, K. & Ernzerhof, M. Generalized gradient approximation made simple. *Phys. Rev. Lett.* **77**, 3865 (1996).

75. Koelling, D. & Harmon, B. A technique for relativistic spin-polarised calculations. *J. Phys. C Solid State Phys.* **10**, 3107 (1977).

76. Ong, P. et al. Electric field control and effect of Pd capping on magnetocrystalline anisotropy in FePd thin films: a first-principles study. *Phys. Rev. B* **89**, 094422 (2014).

## Author contributions

P.K.A. conceived the idea and designed the MTJs. N.D. and J.A.K. fabricated the devices. Y.S. and V.L.-D. performed the measurements and analyzed the data. Q.S. and N.K. performed the ab initio simulations. Y.S., V.L.-D., P.K.A., Q.S., and N.K. wrote the manuscript with contributions from the other authors. All authors discussed the results, contributed to the data analysis, and commented on the manuscript. The study was performed under the supervision of P.K.A.

## Competing interests

The authors declare no competing interests.

## Additional information

**Supplementary information** The online version contains supplementary material available at https://doi.org/10.1038/s43246-022-00310-x.

**Correspondence** and requests for materials should be addressed to Pedram Khalili Amiri.

**Peer review information** *Communications Materials* thanks the anonymous reviewers for their contribution to the peer review of this work. Primary Handling Editor: Aldo Isidori.

**Reprints and permission information** is available at http://www.nature.com/reprints

**Publisher's note** Springer Nature remains neutral with regard to jurisdictional claims in published maps and institutional affiliations.